




## Mechanisms leading to the formation of double-diffusive layers during unidirectional solidification of aqueous $\text{NH}_4\text{Cl}$ solution

Ila Thakur , Shyamprasad Karagadde , and Atul Srivastava <sup>\*</sup>*Department of Mechanical Engineering, Indian Institute of Technology Bombay, Mumbai 400076, India*

(Received 18 November 2021; accepted 27 May 2022; published 22 June 2022)

The phenomenon of unidirectional solidification of binary solutions leads to various flow patterns such as solute fingers, plumes, and double-diffusive layers (DDLs) due to density variations arising out of the coupled effects of thermal and solutal gradients. The present work reports experiments to elucidate the transport phenomena responsible for the formation of DDLs during unidirectional solidification of aqueous  $\text{NH}_4\text{Cl}$  solution in a narrow solidification chamber. The spatiotemporally resolved flow and transported properties associated with the phenomenon have been determined through a combination of nonintrusive techniques. Dual-wavelength interferometry has been used for simultaneous measurement of temperature and salt concentration distributions. Various subprocesses such as convection transients, plume formation, and evolution of DDLs that result in the formation of the stepped structure of solutal-thermal gradients have been mapped through rainbow-schlieren deflectometry. Flow velocities have been quantified using PIV. Based on the whole-field measurements, plausible mechanisms responsible for the development and further evolution of DDLs have been identified. Direct experimental observations revealed the existence of counter-rotating rolls near the chamber sidewalls. Interaction of these convective rolls with the plumes originating from the mushy zone results in a downward inclination of DDLs (towards plume locations), thus giving DDLs a slanted shape instead of their horizontal orientations. The alternate sense of rotation of convective rolls in the adjacent DDLs has been explained through observations made using different experimental techniques. Experimental results are additionally supported with analytical scales of flow parameters such as plume velocity, diameter, the height of DDLs, the downward velocity of DDLs, etc.

DOI: [10.1103/PhysRevFluids.7.063501](https://doi.org/10.1103/PhysRevFluids.7.063501)

### I. INTRODUCTION

Importance of transport phenomena during directional solidification of organic/inorganic binary solutions has been realized by various researchers in the past. When a binary alloy is allowed to solidify, the chemical mixture solidifies at different compositions to that of the melt. This can lead to unstable density gradients (due to the compositional and/or thermal gradients) and thus ultimately causes natural convection to set up [1]. Natural convection can take the form of convective jets (chimneys), which align in the direction of gravitation, and are termed as freckles when finally solidify. A range of experimental and theoretical studies were conducted focused on addressing various subprocesses associated with the solidification phenomena including salt fingers, plume convection, etc. by several researchers [2–9]. It was understood that freckle defects are found in the castings, which usually appear in the form of a long trail of equiaxed grains segregated compositionally. These compositionally segregated regions are also seen in the form of layers

---

<sup>\*</sup>Corresponding author: [atulsr@iitb.ac.in](mailto:atulsr@iitb.ac.in), [atuldotcom@gmail.com](mailto:atuldotcom@gmail.com)

(e.g., stepped structures in oceans, igneous rocks, latte, etc.), which are termed as double-diffusive layers (DDLs). Double-diffusive layers occur due to the presence of double-diffusive convection during the solidification of multicomponent mixtures characterized by different thermal and solutal diffusivities [10–12]. Formation of DDLs can convert an already existing density field into a stepped structure with layers of convective mixing distinguished by a comparatively higher gradient interface [10–16]. The DDLs were studied experimentally by creating a horizontal thermal gradient on a pre-existing vertically varying compositional field in a mixture [10,11,13,17]. Some of the hypotheses, which explain the formation of thermohaline staircases include collective instability [18], metastable equilibria of mixtures [19], negative density diffusion [20], thermohaline intrusions [21], instability of flux-gradient ratio [13], etc. Inclusion of a weak nonlinear analysis along with the conventional linear studies enabled the explanation of complex features of the phenomenology, e.g., direction and circulation of convection cells [22–28].

Magirl *et al.* [29] were the first to demonstrate the presence of double-diffusive layers (DDLs) during directional solidification of an aqueous solution of  $\text{NH}_4\text{Cl}$ . A combination of shadowgraphy [29,30], dye injection, and particle tracking velocimetry techniques were used for qualitative investigation of DDLs in the hypereutectic region of the solution. The formation of horizontal DDLs was attributed to the development of horizontal thermal gradient in the presence of vertical compositional gradient, both resulting from plumes. Vikas *et al.* [3] performed experiments on two hypoeutectic solutions (5% and 15%  $\text{NH}_4\text{Cl}$  with water) using laser interferometry by establishing the calibration curves based on fringe information. Kumar *et al.* [31] performed experiments using Mach-Zehnder interferometry to study the compositional dependency on the onset of double-diffusive layers. A combination of critical solutal and thermal Rayleigh numbers was determined, which were needed for the onset of DDLs [30,32–35]. Kumar *et al.* [36,37] further studied the life cycle of DDLs including onset, formation, disappearance, and recurrence under prolonged freezing conditions in multicomponent mixtures.

There have been several other interesting techniques used for experimentally investigating the convective flow, e.g., microscale-conductivity probe [38], thermochromic liquid crystal (TLC) paint [39], tomography [5], etc. However, the choice of such techniques used for measuring the temperature, composition, and velocity of fluid was restricted. Measurement of composition and temperature using thermal conductivity probes provides data only at certain fixed points of the fluid system and that too in an intrusive manner. In the context of nonintrusive approaches, the majority of them, e.g., shadowgraphy, holography, polarigraphy, interferometry, etc. were used either for the qualitative study of the flow field or their application was limited to measuring only one of the transported parameters, i.e., either temperature or composition. The TLC paint, which generally is applied to the inner wall of the chamber, undergoes color change with changes in temperature and enables the visualization of isotherms [39]. Although this approach is quite useful to determine temperature and velocity in the mushy zone as well, it does not give accurate results of the flow field, as the properties at the wall in contact and farther field can be different. It is well known that the double-diffusive convection is the outcome of the simultaneous variations of composition as well as temperature. In this direction, to circumvent the limitations of the aforementioned techniques and to determine the whole-field distribution of transient composition and temperature simultaneously, dual-wavelength interferometry technique has been utilized in the present work. Recently, Varma *et al.* [40] have utilized a single-shot variant of this technique for the simultaneous measurement of thermal and solutal diffusivities of salt-water solutions.

There have been different experimental, theoretical, and numerical investigations performed to examine the transport phenomena and DDLs during double-diffusive convection in test chambers of medium thickness [36,37,41,42]. However, a number of important details on different characteristics of DDLs are yet to be fully explored. Some of these details include the overall pathway of development of DDLs focusing on different features like shape, size, orientation, inclination, sense of rotation throughout the lifespan of DDLs, the simultaneous mapping of whole-field temperature, and composition in quantitative terms along with the whole-field distribution of velocity field and

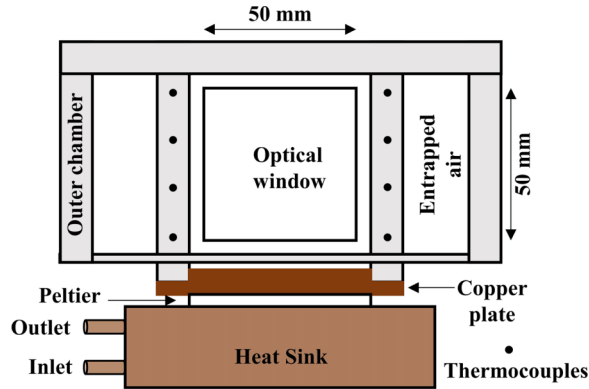


FIG. 1. Schematic setup of solidification chamber.

vorticity as a function of the time transients associated with the evolution from the onset to the disappearance of DDLs.

With this as the motivation, the present work reports an extensive experimental study to investigate the overall pathway of formation of DDLs during the unidirectional solidification of aqueous  $\text{NH}_4\text{Cl}$  solution when cooled from below in a narrow chamber (5 mm thickness). The choice of the narrow chamber is motivated by the fact that a thin chamber is useful to produce conditions that are almost analogous to the theory employed in the majority of the theoretical studies, e.g., zero density gradient in the fluid across the thickness. The cell thickness is optimally decided to ensure sufficient resolution of the fringe patterns during interferometry experiments and to avoid any influence of the vertical wall on the plume flow. Dual-wavelength interferometry technique has been employed for the simultaneous determination of temporal evolution of temperature and composition fields. Transport phenomena associated with the unidirectional solidification of the binary mixture are based on the convection driven by a varying density gradients field caused due to the variation in composition and temperature distributions. In view of this, it becomes important to relate the whole-field velocity scales with that of the transported parameters. To realize this, particle imaging velocimetry (PIV) has been used to quantify the velocity and vorticity fields of the various transport phenomena occurring during the process. In conjunction with these measurements, rainbow-schlieren deflectometry has been employed to interpret the transient evolution of the flow phenomena. A mechanism of the full lifespan of DDLs including different stages, various flow patterns, transport phenomena, and several key characteristics are presented and explained. In this direction, the development of DDLs, existence of convective rolls on the sidewalls of the chamber, realization of a zigzag pattern of DDL instead of the horizontal orientation of interfaces, downward inclination of DDLs towards plume, and alternate sense of rotation of DDLs are some of the important features which have been observed and discussed based on the spatiotemporally resolved nonintrusive measurements.

## II. APPARATUS AND INSTRUMENTATION

### A. Test chamber

The schematic diagram of the test chamber used in the present experiments has been shown in Fig. 1. The inner dimension of the cuboidal solidification chamber, made of 10 mm thick perspex glass with rectangular cross section, is 54 mm in length, 5 mm in width, and 70 mm in height. Two vertical parallel walls of the solidification chamber across the direction of visualization consist of windows having an area of  $50 \times 50 \text{ mm}^2$  and are made up of high optical quality quartz windows (flatness  $\lambda/6$ , thickness 10 mm). These optical windows were placed with the best possible parallel alignment to ensure that the light beam passes without any undesired deviations in the absence of

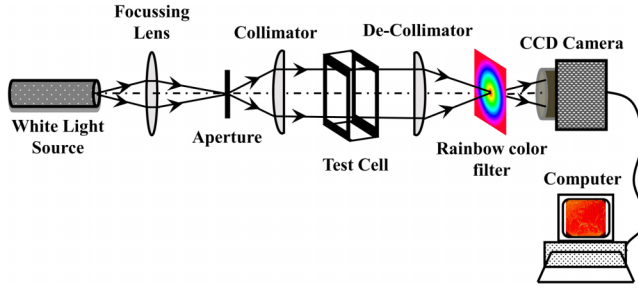


FIG. 2. Optical configuration of rainbow-schlieren deflectometry setup.

density gradients. The bottom surface of the cell consists of a 5 mm thick copper plate, which acts as the thermally active horizontal surface of the solidification chamber. The solidification chamber was covered with an outer cover cell to reduce the heat transfer to the inner solidification chamber from surroundings during experiments. High-quality optical quartz windows were provided in the outer cover cell as well to provide a clear path to the probe light beam and the imaging device. A Peltier module was attached in between the copper plate of the solidification cell and heat sink. A cooling bath circulates a cooler fluid through the heat sink and maintains a fixed temperature on the lower surface of the Peltier module. A DC power source was used to supply power to the Peltier elements in order to create a temperature difference between the two sides of the Peltier surface. In the present set of experiments, the Peltier module was able to create a temperature difference of  $10^{\circ}\text{C}$  when exposed to a 2.5 V DC power supply. This setup has been used to maintain a fixed cooler temperature on the bottom surface of the solidification chamber. Four  $K$ -type thermocouples were attached at different locations on both the sidewalls of the solidification chamber.

### B. Rainbow-schlieren deflectometry technique

Optical configuration of a lens-based rainbow-schlieren deflectometry setup [43,44] is shown schematically in Fig. 2. Image formation in schlieren is based on the principle of refraction, wherein the initially straight traveling light rays (under reference conditions) get refracted as they traverse through a medium with a varying refractive index field. The present setup uses a light source (halogen lamp of 250 W power) integrated with necessary optics to pass a collimated light beam through the test chamber. Various components of the system (white light source, focusing lens, pinhole aperture, collimating lens, test cell, decollimator, rainbow filter, charge-coupled device camera, etc.) are arranged in an in-line manner with the optical axis, as shown in Fig. 2. The light beam traverses through the focusing lens and gets focused onto a  $500\ \mu\text{m}$  pinhole aperture. The light diverging through the pinhole gets collimated into a beam of 50 mm diameter by a collimating lens of 1000 mm focal length.

The optical windows attached on the two opposite sides of the solidification chamber and outer cover cells allow the beam to pass through the region of interest. In the presence of varying refractive-index fields depending on the strength of density gradients, the light beam gets refracted and focused on different color bands of the rainbow filter. The rainbow filter has been placed at the focal plane of the decollimating lens (500 mm focal length). As the white light passes through the different locations of the filter, it acquires different colors that it encounters while passing through it. A CCD camera (pixel resolution of  $2048 \times 1536$  with each pixel being equal to  $3.27\ \mu\text{m}$ ) has been used to record the whole-field images at different time instants. The ascending order of refractive index variation can be directly deduced in the form of successive color variations from red  $\rightarrow$  orange  $\rightarrow$  yellow  $\rightarrow$  green  $\rightarrow$  blue  $\rightarrow$  indigo  $\rightarrow$  violet. For quantitative investigation, the hue values at every pixel of the image can be related to the corresponding angular deflection of light rays caused due to refraction as the beam travels through the medium of varying refractive index



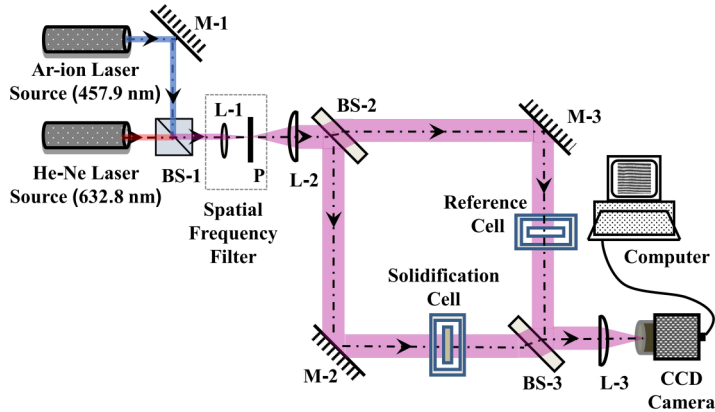


FIG. 3. Optical configuration of dual-wavelength interferometer.

fields, which can further be related to the refractive index gradient and hence, the density values at every pixel. Details pertaining to data reduction methodology for deducing density field from the recorded rainbow-schlieren images can be found in one of our previous works [44].

### C. Dual-wavelength interferometry technique

Dual-wavelength interferometry technique [45] allows nonintrusive, real-time measurements of whole-field temperature and compositional distribution in any given double-diffusive system. The optical configuration of dual-wavelength interferometer, shown in Fig. 3, is quite similar to that of the conventional Mach-Zehnder interferometer. Continuous He-Ne laser (632.8 nm) and Ar-ion laser (457.9 nm) have been used as the coherent light sources. Lasers and a beam splitter (BS-1) are aligned such that both the laser beams coming out from BS-1 become collinear. A spatial frequency filter has been used to magnify the beam, which gets collimated into a 65 mm diameter beam by using a collimating lens (L-2) of 500 mm focal length. A rectangular configuration of optical components (BS-2, M-2, M-3, BS-3) has been arranged by aligning the components at an angle of 45 deg with respect to the laser beam direction.

The collimated beam splits into two parts by passing through the beam splitter (BS-2). The beam splitters have 50% reflectivity and 50% transmissivity. The transmitted part of beam is called the reference beam and the reflected part is termed the test beam. The reflected part of the beam gets reflected from a mirror (M-2) and passes through the solidification chamber and hence called the test beam. The transmitted part of the beam gets reflected from the mirror M-3 and passes through the reference cell and hence is called the reference beam. To record the *in-situ* variations of temperature and composition, the initial composition in the test region and reference region has been kept the same. Both the beams recombine at beam splitter BS-3 and get superimposed with each other. The superposition of two beams creates a combined interference pattern due to the difference in the optical path lengths (difference in phase shift). The interference pattern contains the information of variation of the refractive-index field or density field caused due to the coupled effect of temperature and composition in the solidification cell. Two-color interferograms have been recorded simultaneously using a single Bayer mosaic color CCD sensor with a pixel size of  $3.27 \mu\text{m} \times 3.27 \mu\text{m}$ . Images pertaining to the two colors can be stored in their corresponding color channels, which allows the separation of information related to two wavelengths. Details of the data reduction methodology followed for the determination of composition and temperature distributions from the recorded dual-color interferograms have been presented in the Appendix.

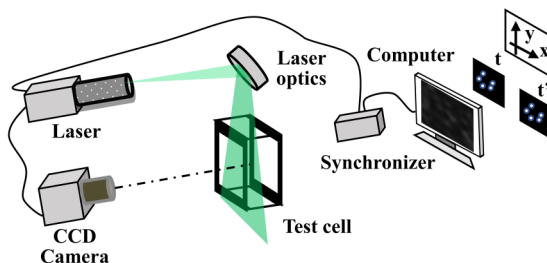


FIG. 4. Schematic diagram of PIV setup.

#### D. Particle image velocimetry

Particle image velocimetry (PIV) has been used to visualize the flow and obtain the instantaneous velocities of convective flow patterns [46,47]. The optical configuration of the PIV setup has been shown in Fig. 4. In the PIV technique, light scattering particles are added to the flow field. The seeding particles should match the fluid properties well so that they follow the flow satisfactorily. The micron-sized seeding particles used in the present study are glass beads. A double pulsed Nd-YAG laser has been used as the light source. The laser beam is converted into a light sheet using a suitable laser sheet optics. The resultant light sheet is made to pass through the flow field. The laser beam is illuminated twice in a short time interval of  $\Delta t$ . A synchronizer acts as an external trigger for both the camera and the laser. It controls the time between the two exposures and the placement of laser shots with respect to the camera's timing. The two exposures of laser light are recorded in the form of two consecutive frames by a high-resolution digital camera. Two representative frames are shown in Fig. 4 at time  $t$  and  $t'$ . The high-resolution digital cameras enable each exposure to be isolated on its own frame for cross-correlation analysis. The particle images can be broken down into many small interrogation windows. The average particle image separation is determined by cross correlation and localization of the correlation peak. Velocity components and correspondingly vorticity components can be determined by obtaining the displacement of the seeded particles in a particular time  $\Delta t$ .

### III. RESULTS

Experimental observations are presented in the form of two-dimensional (2D) rainbow-schlieren images, dual-wavelength interferograms, and PIV images recorded during the unidirectional solidification of the aqueous solution of water with 28 wt.% of  $\text{NH}_4\text{Cl}$ . Considering the thermo-physical properties of the binary solution employed, the thermal and solutal Prandtl numbers correspond to 8.9 and 252, respectively, near room temperature. The eutectic composition and eutectic temperature of the aqueous  $\text{NH}_4\text{Cl}$  solution used in the present set of experiments are 19.7 wt.% and  $-15.4^\circ\text{C}$ , respectively. As the bottom surface of the solidification chamber is maintained at a temperature ( $T_B \sim -18^\circ\text{C}$ ) below the liquidus temperature of the binary solution, the solidification begins from the bottom region. The choice of bottom cooling temperature has been made to allow the solution to freeze in the solid and predominantly in the mushy region of the phase diagram. Experiments using different nonintrusive techniques were performed by maintaining similar experimental and environmental conditions.

#### A. Rainbow-schlieren deflectometry observations

The temporal evolution of solidification and natural convection setup in the liquid domain is captured in the form of time-lapsed schlieren images. Decreasing strength of density gradients in schlieren observations gets manifested into the redistribution of colors, with the shades of violet representing strong density gradients while the red shade representing negligible or minimum strength

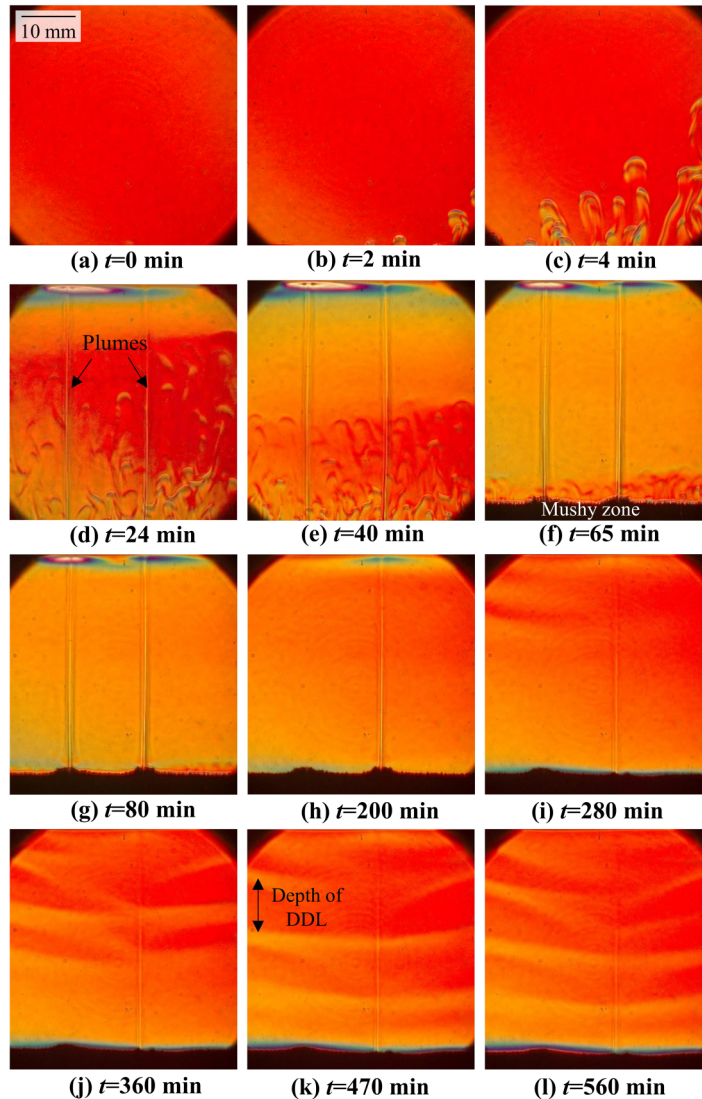


FIG. 5. Rainbow-schlieren observations at different instants of time.

of such gradients in the V.I.B.G.Y.O.R. series (refer to Fig. 2). Considering that the horizontal orientation of the double-diffusive layers is expected in the present experiments, a horizontal color band filter has been chosen to capture the vertical gradients in the flow field. At  $t = 0$  the solution in the test cell is exposed to the bottom temperature of  $-18^\circ\text{C}$ , which is maintained throughout the course of experimental run time. The solution was kept in the setup and was allowed to get stabilized before exposing it to the bottom temperature. With reference to Fig. 5, at  $t = 0$ , in the absence of any significant density gradients in the liquid, a uniform red color distribution is to be observed in the field of view [Fig. 5(a)]. As the solidification begins, the ratio of  $\text{NH}_4\text{Cl}$  and water changes in the liquid as well as in the solid. As part of the solidification process, water gets rejected in the liquid region as solute and the salt composition increases in the solidified region. Fact that the visualization window is 15 mm above the bottom cooling surface, the solidified region (like mushy zone) is visible (in the form of a bottom black region in Figs. 5(e)–5(l)) only after it grows above

15 mm. The rejection of low-density water into the liquid region causes the buoyancy force to initiate natural convection. Also, the smaller salt diffusivity compared to high thermal diffusivity allows the upward moving fingers to sustain buoyancy as they retain their composition while absorbing heat from the surroundings. Initiation of salt fingers can be seen in Fig. 5(b) at around  $t = 2$  min in the form of yellow-green patterns on a nearly uniform red color background. The solute fingers grow with time and their number increases. Initial convection transients can be seen in Fig. 5(c), which cause intermixing of bulk fluid with the lighter and cooler fluid rising from the bottom.

Gradually, the strength of convective solute fingers reduces and some convective fingers originated from the mushy zone develop into well-defined lower-density jets (plumes). The formation of a stable plume is primarily driven by the presence of a permeable mushy zone, i.e., the solid-liquid mixture that allows solutal rich liquid (less dense) to move upwards from the mushy zone, creating a channel inside the mushy zone and a long-standing streamer (identified as a plume) in the liquid region. These plumes are further fed by the entrainment of additional solute-rich liquid from the neighboring regions in the mushy zone. Unlike salt fingers, the plumes are sufficiently stable and strong enough to reach directly to the top surface of the test cell without getting mixed with the bulk fluid in between. Two such stable plumes can be seen in Fig. 5(d) as the straight vertical color shades, as indicated, which transport the cooler but lighter density fluid from the bottom to the top of the test cell. This excess of lighter fluid on the top can be seen in the form of color (hue) redistribution in the top region, indicating the localization of higher density gradients. There is a slightly white region just at the top of the left plume in Fig. 5(d), which occurred due to the presence of very strong gradients at that location, which could not be accurately captured through the rainbow filter as the light rays fall beyond the rainbow filter. The upper higher gradient region spreads over a large portion of the visualization area with time. The distinct color contrast seen in the top region of Fig. 5(e) represents the presence of strong density gradients due to the fresh fluid reaching upwards through plumes and the bottom red-colored region now is occupied by weaker solute fingers. Convective solute fingers become weaker with time and finally disappear, as can be seen in Figs. 5(f)–5(h).

The indication of the onset of double-diffusive layers can be seen in Fig. 5(i) ( $t = 280$  min). Also, there is only one plume left at this time instant. The horizontal patches of yellow shade can be interpreted as the interface of DDL. The initiation of DDL has been found to occur in the upper part of the chamber and two distinct DDLs can be seen in Fig. 5(i). Eventually, the number of DDLs increases and descends towards the bottom. While moving downwards, the DDLs disappear as soon as they come into contact with the mushy zone-liquid interface. Newer DDLs originate in the upper half of the chamber and continue moving downwards. Figures 5(j)–(5l) show the presence of multiple DDLs in the field of view. Images were captured for 580 min from the beginning of the experiment.

It is interesting to note that the DDLs formed in the present system are not exactly horizontal, instead, these layers are slightly tilted (downwards) towards the plume location. The maximum number of plumes formed in water-28 wt.%  $\text{NH}_4\text{Cl}$  solution is 4. Although the velocity of fluid moving upwards varies with time, the maximum plume velocity obtained in this case is 1.5 mm/s. Plume velocity has been calculated by tracing the path of the fluid structure from one-pixel location to another. Once the DDLs are formed during the experiment, the depth of DDLs can be obtained by a similar way of pixel tracking. The downward propagation speed of DDLs decreases with time. The maximum movement speed of DDLs in the present case was obtained as 0.007 mm/s and the minimum (towards the end of the experiment) as 0.002 mm/s. Figure 6 shows the number of DDLs with time and their movement. In Fig. 6, the  $y$  axis represents the height of the visualization window and the  $x$  axis represents the experimental run time. Different curves represent the time variation of the height of the different double-diffusive layers, as shown by the legend. When the layers move downwards, the bottommost layer gets ruptured as soon as it reaches the mushy-zone interface, at the same time other DDLs originate from the top and move downwards. As the DDLs come in contact with the mushy zone-liquid interface, they get vanished along with the remelting of the mushy zone. Due to the remelting of the dendritic region, the height of the mushy zone (solidified

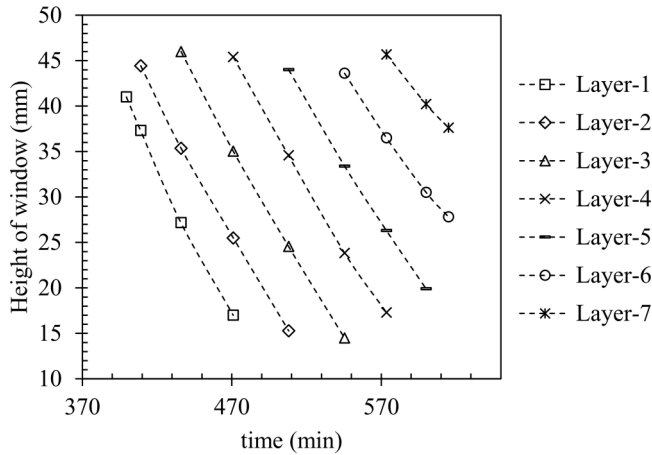


FIG. 6. DDLs position at different time instants.

region) reduces, which can be seen in Figs. 5 (j)–5(l) after the formation of DDLs. The reduction in the number of DDLs with time leads to an increment in the depth size. The depth of the DDLs increases from around 6.3 mm at 340 min to 14.3 mm towards the end of the experiment. During this time period, the number of DDLs also reduce.

Thermocouples have been employed on the sidewalls of the solidification chamber at different heights. The time history of temperatures measured by the thermocouples is shown in Fig. 7. The lowest curve in Fig. 7 shows the temperature of the thermocouple that is attached to the bottom copper plate of the solidification chamber. The rest of the four curves show the temperature of the liquid at different heights of the solidification cell. The temperature boundary condition required for the quantitative analysis of the dual-wavelength interferograms has been taken as the temperature of the topmost thermocouple inserted on the upper surface of the visualization window.

### B. Whole-field concentration and temperature measurement

Since the process of unidirectional solidification of  $\text{NH}_4\text{Cl}$ -water binary mixture involves double-diffusive convection, it results in the setting up of the compositional as well as thermal gradients and hence it becomes important to quantify these scalar parameters. Figure 8(a) shows the interferogram

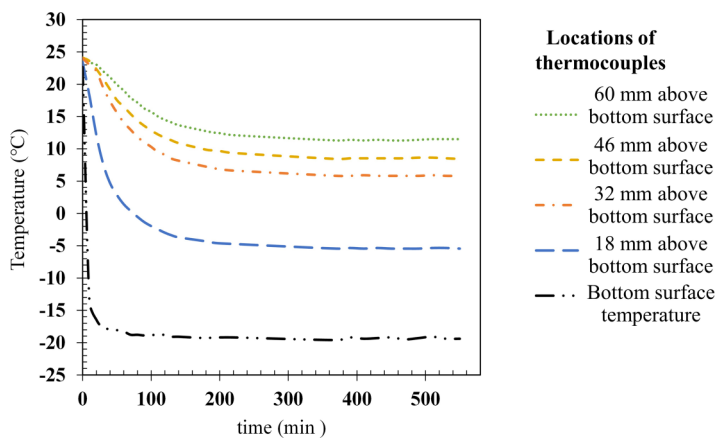


FIG. 7. Thermocouples based temperature variation as a function of experimental run time.



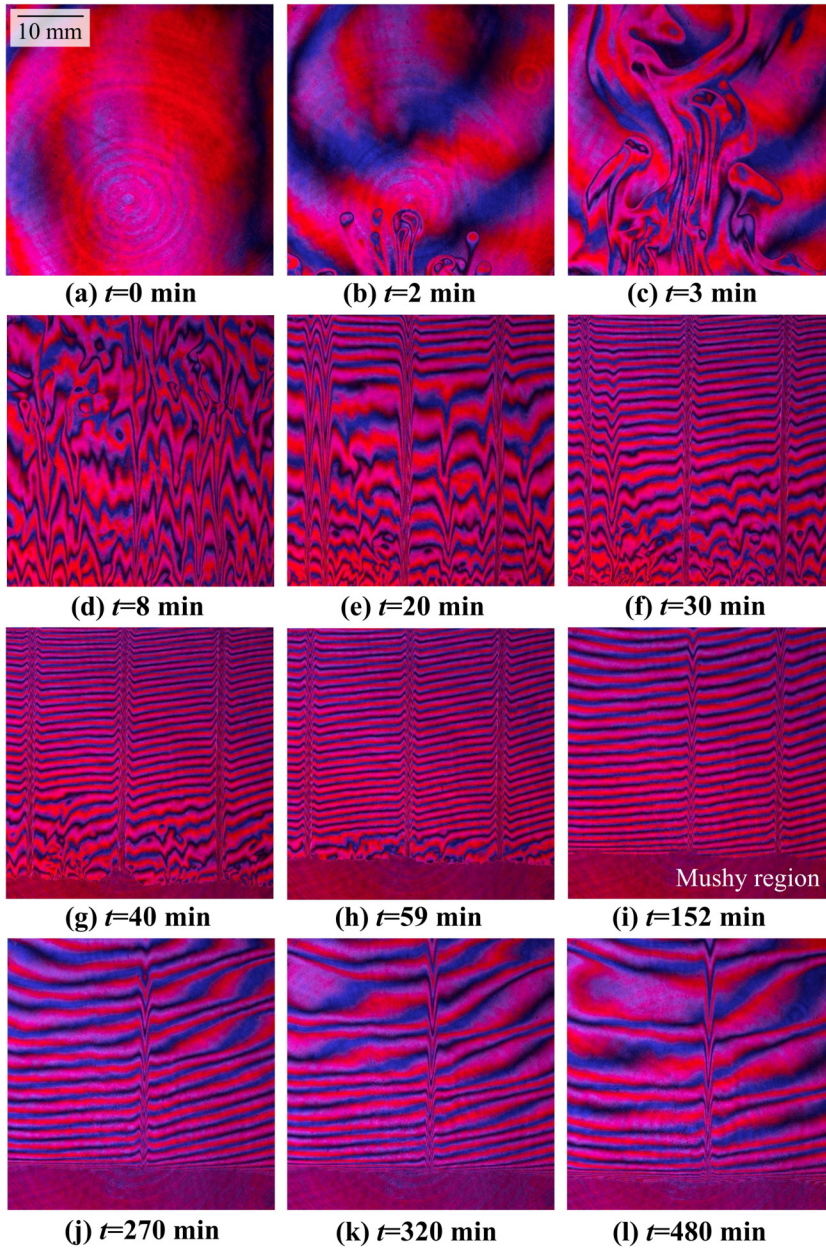


FIG. 8. Dual-wavelength interferograms during the experimental run time.

at  $t = 0$  min wherein almost no temperature and/or concentration gradients are to be seen as the phenomenon has not yet been initiated. As discussed in the previous section on schlieren-based observations, the onset of natural convection takes place due to the rejection of low-density water into the liquid region upon solidification. Figure 8(b) shows some of the solute fingers formed in the presence of buoyancy forces. Figure 8(c) shows the evolution of natural convection transients and random intermixing of solute fingers with the bulk fluid. It is to be noted that since the solidification process begins due to the bottom surface cooling of the binary solution, ideally one expects the



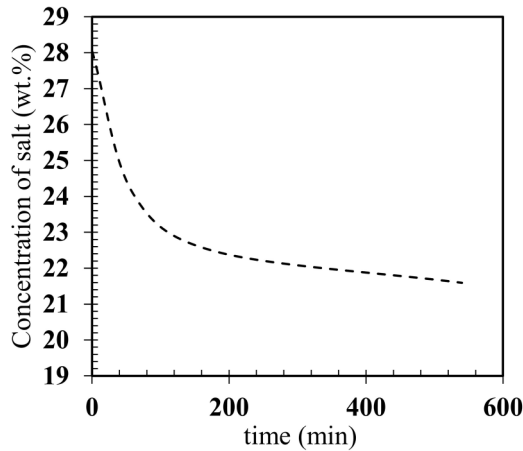


FIG. 9. Variation of composition of binary solution on the top of the chamber during the experimental run time.

localization of closely spaced horizontal fringes in the vicinity of the bottom (cooler) surface of the chamber due to strong thermal gradients in this region. However, some disturbances that are to be seen in these fringes are because of the compositionally driven solute fingers and their intermixing with the bulk fluid. This condition has been captured in the interferogram shown in Fig. 8(d) at  $t = 8$  min. The fluid brought by plumes spreads over the top region of the test cell, as its effect can be seen in the form of relatively closely spaced (dense) fringes on the upper portion of the test cell [Fig. 8(e)]. As explained on the basis of schlieren observations, the spatial stretch of the region of fresher fluid (brought through plumes) covering the upper portion increases with time. Also, the bottom region of fluid containing the convection transients reduces with time. Continuous reduction of the lower sparsely spaced fringe region can be seen in Figs. 8(f)–8(h).

Figure 8(i) shows the visualization window getting completely filled with newer fringes originating from the top. A clear indication of the appearance of DDL has been found at around  $t = 270$  min, as shown in the interferogram in Fig. 8(j). The interferogram shows the division of high and low gradient regions of DDLs in the form of closely and sparsely spaced distributed fringes, respectively. The layers start to originate from the right side of the visualization window [Fig. 8(j)] and develop with time, spreading in the lateral direction across the width of the chamber (between its two sidewalls). Some layers can be clearly seen in Fig. 8(k) with a single plume existing in the field of view. The interferograms are recorded till around 500 min and the corresponding interferogram has been shown in Fig. 8(l) (at  $t = 480$  min).

As part of the quantitative analysis, for obtaining the boundary condition of the compositional field, a small amount of fluid parcel has been extracted from the top of the cell. Using a multi-wavelength refractometer, the composition of the collected fluid parcels on the top surface of the test cell has been measured at different time instants. The time variation of concentration at the top of the solidification chamber has been shown in Fig. 9. As expected, the composition is higher in the beginning and gradually reduces with time. The observed trend is expected since as the solidification takes place, water gets rejected into the bulk fluid, reaches the top through plumes, and keeps diluting the liquid composition in the top region of the chamber. Also, the solidification rate is quite high at the beginning, which implies a higher rate of change of composition in the beginning (Fig. 9).

Interferograms for analysis have been chosen at three different time instants. Figures 10(a), 10(d), and 10(g) show the dual-color interferograms at 270, 320, and 480 min, respectively. Corresponding whole field maps of temperature distribution have been shown in Figs. 10(b), 10(e), and 10(h), while those for salt composition have been presented in Figs. 10(c), 10(f), and 10(i). The temperature in

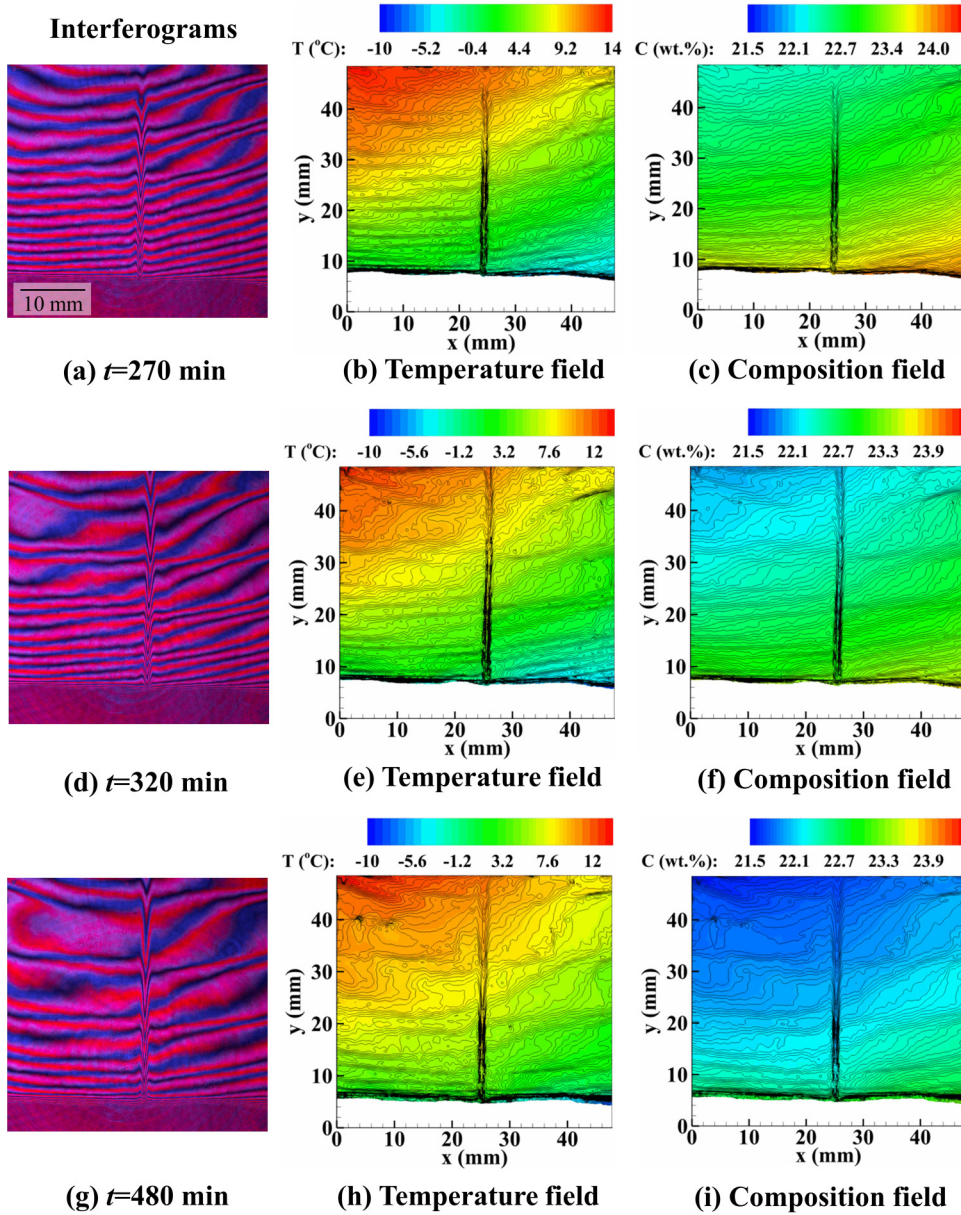


FIG. 10. (a) Dual-color interferogram at  $t = 270$  min, (b) temperature field at  $t = 270$  min, (c) composition field at  $t = 270$  min, (d) dual-color interferogram at  $t = 320$  min, (e) temperature field at  $t = 320$  min, (f) composition field at  $t = 320$  min, (g) dual-color interferogram at  $t = 480$  min, (h) temperature field at  $t = 480$  min, and (i) composition field at  $t = 480$  min.

the top region is relatively higher and reduces towards the bottom of the solidification chamber. Correspondingly, the salt composition is lesser on top and higher towards the bottom. Based on the quantitative analysis, at 270 min (at the onset of DDL), the maximum temperature on top and minimum temperature in the bottom region was obtained as 14 and  $-10$  °C, respectively. On the other hand, the minimum composition on top and maximum composition on the bottom were obtained respectively as 22.4 and 24.2 wt.%. Gradually, the temperature and composition

both reduce in the field of view and the values at  $t = 480$  min have been shown in Figs. 10(f) and 10(i). The dual-color interferometry-based observations have successfully captured the salient features of the spatiotemporally resolved transported parameters during the process of unidirectional solidification of the binary mixture. It is pertinent to mention here that while the quantitative data shown in Fig. 10 successfully captures the distribution of temperature and concentration fields (including the range of variations of these parameters) in the bulk of the solidification chamber, it shows some inherent discrepancies near the mushy zone-liquid interface and also within the plume. These discrepancies are to be attributed to the presence of a large number of closely spaced fringes in these localized regions (near the mushy zone and inside the plume), which are difficult to resolve. This is an inherent limitation of the interferometry technique when applied to applications involving high gradients. However, irrespective of these limitations in some localized high gradient regions, the knowledge of the real-time variation of the transported parameters enables the development of a deeper understanding of the phenomena by providing the real-time values, which can be useful for numerical and/or analytical analyses.

### C. Whole field velocity scales

Observations made through PIV provide direct support to the schlieren and dual-wavelength interferometry-based experimental results and enable a deeper understanding of the overall behavior of DDLs in narrow chambers, as employed in the present experiments. The transient evolution of the velocity field of liquid above the mushy zone-liquid interface is shown in Fig. 11. Figure 11(a) shows the velocity field for the initial convective solute fingers and their mixing with the bulk fluid at  $t = 20$  min. Natural convection was seen to initiate at around 2 min, an observation that is in line with the behavior found in rainbow-schlieren deflectometry and dual-wavelength interferometry-based experiments. During this phase, the velocity of solute fingers was found to be around 0.35 mm/s. Figure 11(b) shows the velocity scales of convective solute fingers after 40 min past the start of the experiments. Suppression of convective fingers with time can be seen in Fig. 11(b), a phenomenon that has earlier been explained based on schlieren and interferometric observations. The velocity scales in each of the images shown in Fig. 11 are different, which are shown using the legends placed over the top of each image. Arrows show the relative magnitude and direction of velocity at different locations in any given image. While solute fingers move upwards, for mass conservation, some mass gets transferred from top to the bottom surface of the solidification chamber. This explains the observed phenomenon wherein along with the upward moving solute fingers, there is a downward flow at some locations. The PIV data in Fig. 11(c) shows the number of stable plumes formed as 2. The velocity of plumes as retrieved through PIV analysis is found to be a little lesser (0.2 mm/s) than that determined using the schlieren technique. One of the reasons for this difference can be the location of plumes. The plumes generally form at one of the walls, which makes it difficult to illuminate the laser sheet at the plume without interfering with the wall. Also, the density of PIV tracer particles in the plume is far lesser than the bulk fluid. One of the reasons behind it can be the fact that there is a high chance of particles getting obstructed in the mushy zone when they move towards the plume in the mushy zone. When the laser sheet was focused on a different plane away from the plume, the bulk velocity could be captured, as shown in Fig. 11(d). Signatures of DDLs can be seen in Fig. 11(e) at  $t = 260$  min in the form of some well-defined horizontal velocities (red-colored region) with an alternate sense of motion. Figures 11(f) and 11(i) clearly show the formation of convection rolls and the velocity patterns near both sidewalls result in the formation of different rolls at different heights. The direction of rotation of fluid particles in the convective cells can be seen by the velocity vectors and is highlighted by white loops drawn over Fig. 11(f).

Figure 11(h) shows two convection rolls near the left wall and three convection rolls near the right wall. The sense of rotation of the left-side rolls is clockwise and that of the right-side rolls is anticlockwise. The observed sense of rotation can be confirmed by further studying the vorticity field at the corresponding time instants. Also, it can be seen that the left-side rolls merge with right-side rolls. When one left-side convection roll merges between two right-side rolls, it creates



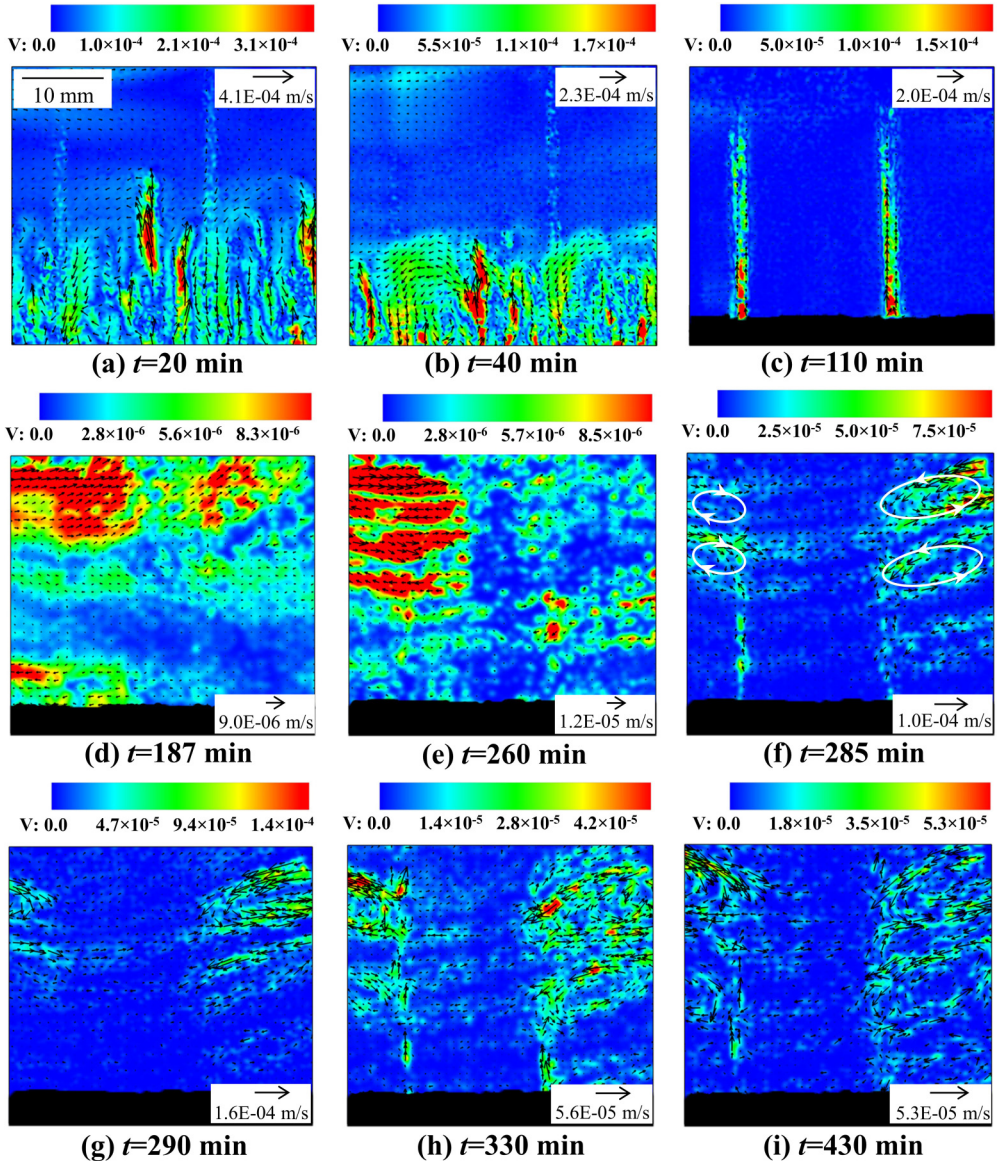


FIG. 11. Velocity components (m/s) during the unidirectional solidification of water-28wt.%  $\text{NH}_4\text{Cl}$  solution.

DDLs with an alternate sense of rotation. The convection rolls were also found to be inclined downward near the plume. The origin of new DDLs from the top, downward movement of DDLs and disappearance of DDLs from the bottom have also been observed and are in agreement with the earlier observations made from rainbow-schlieren deflectometry and dual-wavelength technique. With time, these velocity scales become weaker [Fig. 11(i)].

Figure 12 shows the vorticity field corresponding to the velocity field shown in Fig. 11. The vorticity field further confirms the sense of rotation of liquid at different locations and is particularly important in the cases where convection rolls are formed. The green region in all the images in Fig. 12 shows the absence of any rotational movement. Images show blue color (negative values) when the sense of rotation is anticlockwise and red color (positive values) when the sense of rotation

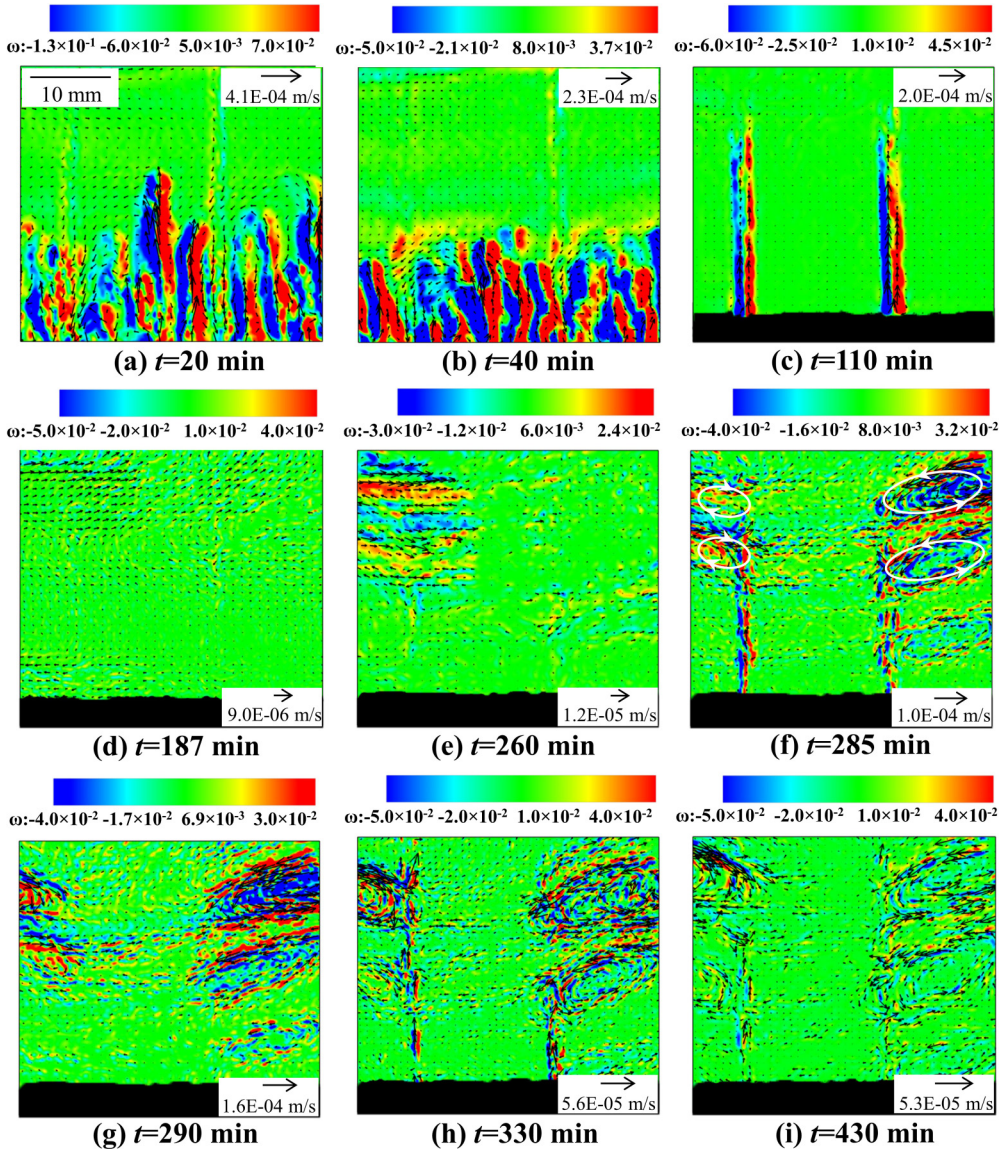


FIG. 12. Vorticity components (1/s) during the unidirectional solidification of water-28 wt.%  $\text{NH}_4\text{Cl}$  solution.

is clockwise. The exact extent of the magnitude of vorticity can be understood on the basis of the legend shown corresponding to each image. Similar to Fig. 11, arrows indicate the relative extent of velocity and direction of motion at any given time instant. Figures 12(a) and 12(b) show the vorticity field during the initial convection phase while Fig. 12(c) shows the vorticity field when 2 stable plumes exist in the field of view. When the fluid moves from bottom to top in the form of solute fingers/plumes, the resultant shear effects create some inertia in the neighboring fluid adjacent to it. Due to the induced shear, the fluid on the left side of the volume experiences an anticlockwise rotation and the right-side fluid experiences a clockwise rotation. Such patterns can be seen in the form of a blue region on the left and a red region on the right of each plume, respectively. When a different plane was focused [Fig. 12(d)], there was a relatively lesser velocity. In the absence of any

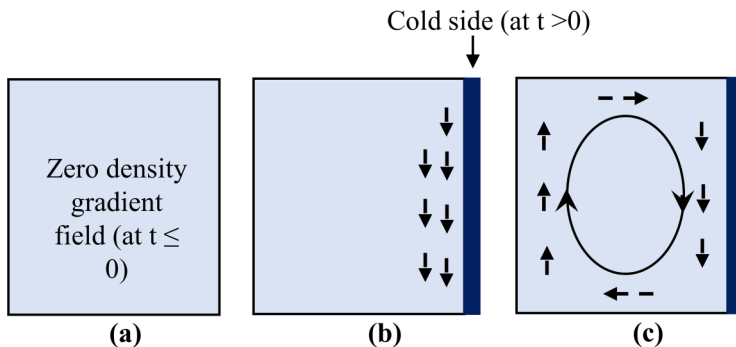


FIG. 13. Convection roll formation in a zero gradient density field by exposing a lateral thermal gradient.

plumes/DDLs, the vorticity is quite less, as shown by a predominantly green region. Figure 12(e) shows the vorticity field and indicates the initiation of DDLs. The alternate blue and red region on the left side of Fig. 12(e) shows the presence of vorticity and the sense of rotation of fluid in DDL. Figures 12(f) and 12(g) show the observations captured at two different planes at 285 and 290 min, respectively. Figure 12(f) captures the plane of the plume (and hence indicates the presence of plumes), and Fig. 12(g) corresponds to the plane that is away from the plume plane (and hence does not indicate any sign of plumes). Figures 12(f)–12(i) shows the vorticity field that indicates the presence of convection rolls. The inner region of the left side rolls [Fig. 12(g)] shows a red shade confirming the clockwise sense of rotation. On the other hand, the inner region of the right-side rolls shows the blue region indicating an anticlockwise sense of rotation. The rolls merge leading to the formation of DDLs with an alternate sense of rotation.

#### IV. DISCUSSION

During unidirectional solidification of aqueous  $\text{NH}_4\text{Cl}$  solution, various phenomena have been observed. Right at the onset of the process, initial convection transients occur with velocity scales in the range of 0.7 to 2 mm/s. The overall effect of thermally stable and compositionally unstable convective gradients leads to the initiation of natural convection, which finally results in plumes and DDLs. The continuous transfer of low-density fluid from bottom to top through plumes and the disappearance of random smaller solute fingers leads to a vertical density variation (higher density on the bottom and low on the top). This vertically varying density field gets converted into a stepped structure of DDLs with an interface in between every two layers. The downwards movement speed of DDLs has been determined to be 0.007 mm/s at the beginning, which changes to 0.002 mm/s towards the end. The total number of DDLs and their downward movement speed reduces with time. Correspondingly, the width of DDLs also increases and the corresponding increment has been found as around 6.3 mm in the beginning to 14.3 mm in the end.

##### A. Mechanism of formation of DDLs

The present discussion addresses the mechanism of formation of DDLs during bottom cooled unidirectional solidification of an aqueous solution. The mechanism explained in the present work is primarily based on the explanation given for double-diffusive instability by several authors [11,23,26,27], wherein they used a setup with a vertically varying density field with a heated sidewall, the detailed insights of which are schematically depicted in Figs. 13 and 14. The analogy used in Figs. 13 and 14 makes the basis for the formation of DDLs in the present work and is explained using Fig. 15.

Figure 13 schematically presents the convective flow field setup in a cavity where one of the sidewalls is cooled and the bulk fluid is initially characterized by a uniform density field (instead of



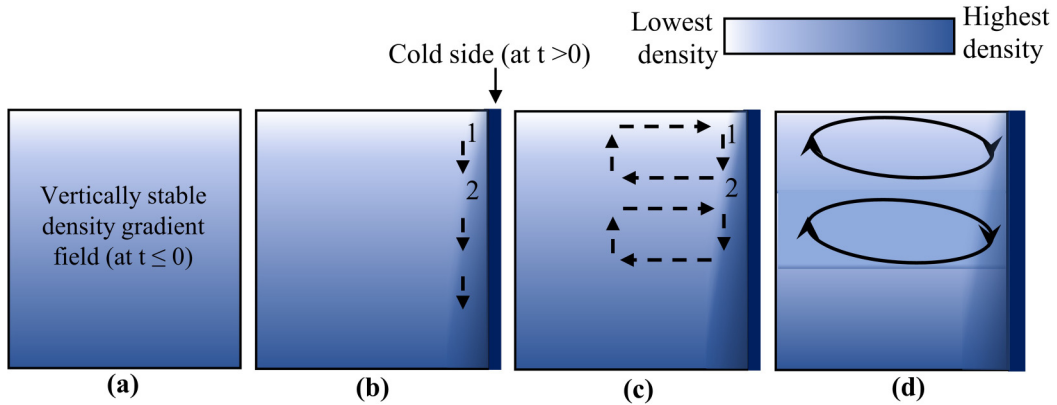


FIG. 14. Schematic diagram showing formation of DDLs in a pre-existing vertically varying compositional field by exposing a lateral thermal gradient.

a pre-existing vertically stable density gradient), Fig. 13(a). When the right-side wall is exposed to a cooler temperature, the temperature of the fluid near the sidewall decreases due to thermal diffusion. Cooling of the fluid in the close vicinity of the sidewall increases its density, which ultimately leads to a shear-induced downward movement of fluid near the wall. As the cooler fluid moves from top to bottom [Fig. 13(b)], neighboring fluid particles from the top portion of the cavity compensate the downward moving cooler fluid to ensure mass conservation. The resulting movement of the fluid leads to the formation of a single convective roll pattern inside the whole cavity [Fig. 13(c)]. So, no multiple convective rolls (and DDLs) can form in the absence of any pre-existing vertical density field.

Figure 14 schematically depicts the convective fluid movement in a fluid medium that initially has a vertically stable density field [Fig. 14(a)] and the right wall of the cavity is cooled at  $t > 0$ . The boundary layer on the right wall leads to a shear-induced downward movement of the cooler fluid [Fig. 14(b)]. However, unlike the fluid domain in Fig. 13, where there is no increasing obstruction in the downward direction, the downward movement of fluid particles in Fig. 14 gets restricted/resisted by the increasing strength of the composition gradients in the downward direction. The fluid particles move downwards as their density increases because of the horizontal thermal diffusion, but the extent of their descent is restricted to the point where the density increment due to horizontal thermal diffusion gets balanced by the increase in their density due to the oppositely oriented vertical compositional variation and hence, any further downward movement stops. It can be said that the fluid domain experiences vertical gradients (pre-existing vertical compositional gradient), horizontal gradients (thermal gradients due to side-wall cooling and compositional gradient due to the vertical movement of particles near the side-wall, which retain their compositional identity), and vertical shear. In Fig. 14(b), the fluid particles from Location 1 move up to Location 2 and then get horizontally shifted inside. This way a convection roll pattern of certain depth develops. Other particles below Location 2 also experience the same process and similarly, other convective rolls also get developed [Figs. 14(c) and 14(d)]. Due to the fluid movement inside each convective roll, the properties (composition and temperature) inside the rolls get homogenized and a thin interface, which separates any given two convective rolls, manifests itself into a comparatively higher gradient region. The direction of flow of fluid inside such different layers is of the same orientation [clockwise sense of rotation, Fig. 14(c)]. As shown in Fig. 14(c), when the right-side wall is cooled, the convective patterns have a clockwise direction. This explains the mechanism of the development of double-diffusive layers in a fluid medium when one of the sidewalls of the chamber is cooled and the fluid has a pre-existing vertical density gradient field [15,23,26,27].

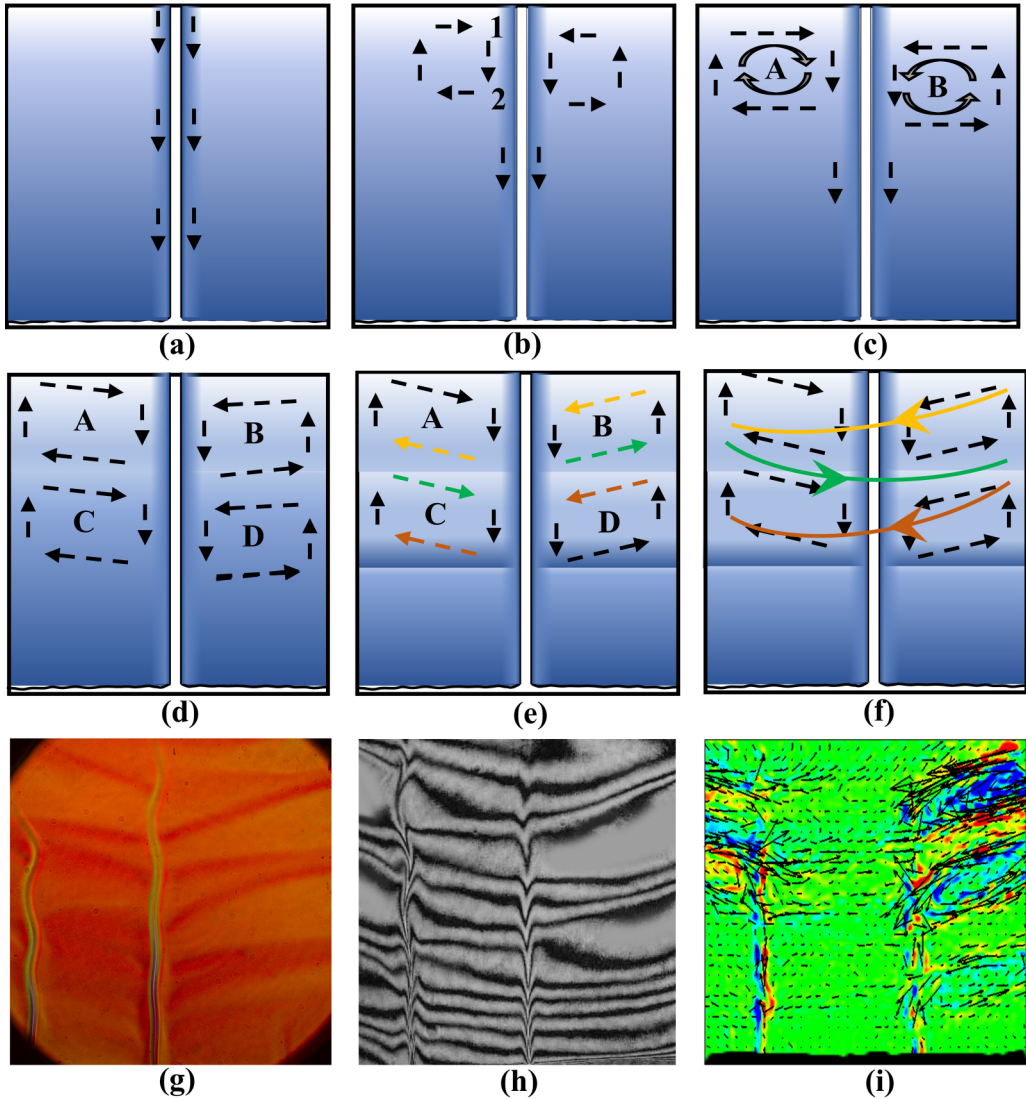


FIG. 15. Schematic diagram to show different stages for the formation of DDLs: (a) Vertically stable compositional gradient with lateral cooling by plume, (b) initiation of convection rolls, (c) existence of convection rolls A and B, (d) formation of convection rolls C and D, (e) direction of movement of fluid inside convection rolls, (f) expanded DDLs, (g) representative schlieren observation, (h) representative interferometric observation, and (i) representative vorticity field with velocity vector.

The above discussion, made on the basis of flow configurations shown in Figs. 13 and 14, has now been used to explain the phenomenon of DDL formation (double-diffusively driven instability), as observed based on the combination of nonintrusive imaging techniques employed in the present work. One of the major differences between the situation depicted in Fig. 14 and the actual solidification experiments of the present work lies in the way of existence of horizontal thermal gradients in the respective fluid medium. In the present solidification experiments, the horizontal thermal gradients are formed as a result of the process of thermal diffusion occurring due to the existence of cooler plumes compared to the bulk fluid [Fig. 15(a)]. As the thermal diffusivity is about 2 orders of magnitude higher than the solutal diffusivity, thermal diffusion takes place faster

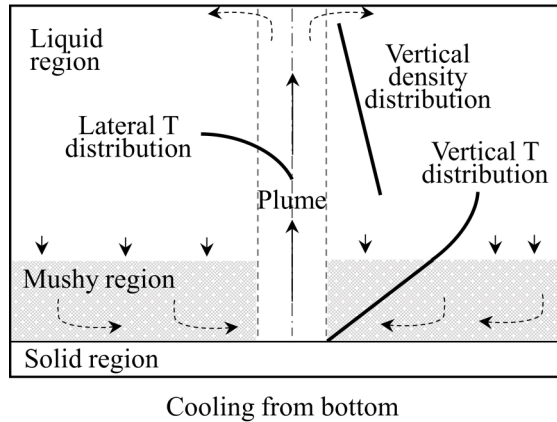


FIG. 16. Schematic diagram representing the physical processes before the onset of DDLs.

and a horizontal thermal gradient quickly sets up. The unidirectional solidification experiments show that the vertical density field sets up due to bottom cooling and movement of low-density fluid from bottom to top through plumes, which eventually spreads in the bulk. Thus, there are three components; pre-existing vertical compositional and thermal gradients, induced horizontal thermal and compositional gradient, and vertical shear. As a result, the system is characterized by various physical subprocesses that occur simultaneously just before the onset of DDLs, as schematically depicted in Fig. 16. Once the downward force due to thermal diffusion gets balanced by the opposing vertical compositional field, the downward movement of the fluid particles stops at that particular depth [from 1 to 2 in Fig. 15(b)] and the fluid particles spread around that particular horizontal level [2 in Fig. 15(b)]. As the plume exists somewhere in between the two sidewalls, two convective rolls are expected to form at any particular height, one on each side of the plume. In this way, small convection cells get set up, as shown schematically in Fig. 15(b). It is to be noted here that in the present discussion, only two sides are active as the test chamber is a narrow cell, restricting the fluid movement along its thickness.

These convective cells become stronger with time and expand on both sides of the plume. Figure 15(c) shows two convective rolls A and B on either side of the plume. Other particles below the location of plane 2 experience the same process and more rolls below A and B are formed [Fig. 15(d)]. One of the key features of these rolls is that they get inclined downwards near (towards) the plume. This trend can be explained by the fact that as the thermal diffusivity is higher than solutal diffusivity, the temperature of the fluid particles moving towards the cooler plume keeps on reducing, and hence their density increases, which explains a slight downward inclination of the two roll like structures towards the plume.

Another key feature of these convective rolls is the direction of rotation of the fluid inside these rolls. The convective rolls near the left wall move in a clockwise direction as the cooler boundary for these rolls are on the right side (near the plume). The convective rolls near the right wall move in an anticlockwise direction as the cooler boundary for these rolls are on the left side (near the plume). Although the solidification chamber is a narrow cell and hence two rolls form on either side of the plume, the plume diameter is not large enough to separate these rolls distinctly (the plume diameter was found to be around 1 mm, and the chamber thickness is 5 mm). Once the convective rolls near each wall form, they try to spread throughout the cell width. Following this mechanism, the convective rolls take the form of DDLs and spread throughout the breadth of the solidification chamber. Figures 15(e) and 15(f) shows the expansion of convective rolls throughout the chamber boundaries. Figure 15(e) shows the similar direction of fluid movement in rolls A, B, C, and D with the same colors. The fluid particles moving along the yellow direction of convective roll

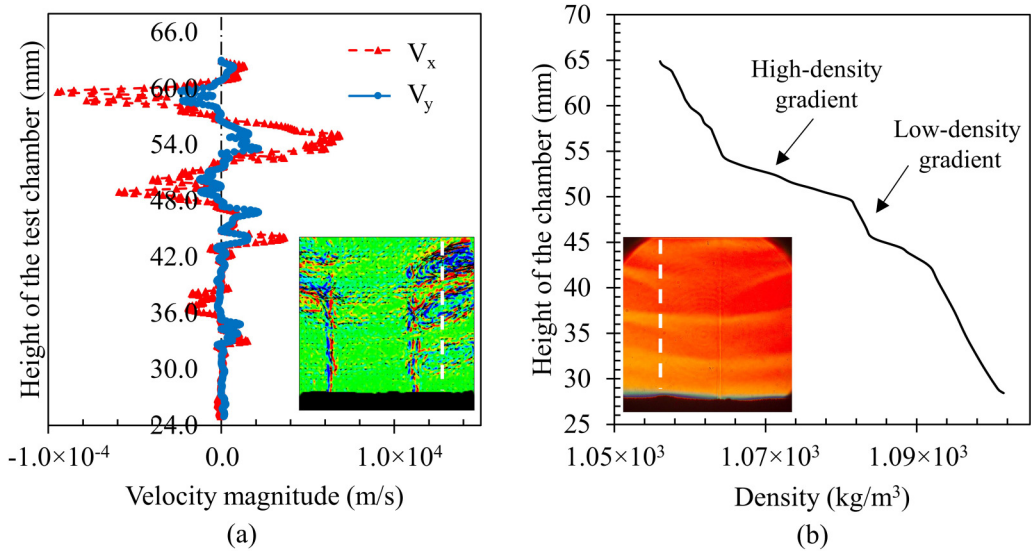


FIG. 17. Plot of (a)  $x$  and  $y$  component of velocities ( $V_x$  and  $V_y$ ) and (b) density profile along the height of the fluid domain (the vertical sections considered to plot the profiles are indicated as dashed line in both the PIV and schlieren images shown in the inset of each figure).

B expand towards the left wall moving along the yellow direction of convective roll A. Similarly, the fluid moving along the green and brown colors also expands throughout the chamber [Fig. 15(f)]. Following this orientation, one roll from the right wall having an anticlockwise sense of rotation penetrates between two rolls from the left wall with clockwise rotation. This explains the possible reasons behind the expanded adjacent DDLs to have an alternate sense of rotation.

The experimental images shown in Figs. 15(g), 15(h), and 15(i) indicate that the DDLs do not have the same (uniform) depth throughout the width of the chamber. The PIV images in Figs. 11(f)–11(i) and 12(f)–12(i) showed that not all the fluid particles in a DDL penetrate throughout the width of the cell. The bulk of the fluid particles of DDL originated from the left wall rotate and complete the circle on the left side only. Only a few fluid particles reach the opposite wall resulting in a lesser DDL thickness on the opposite wall. Similarly, most of the fluid particles of DDLs originated near the right wall, complete their cycle on the right side itself. This explains the observation that the right-side originated convective rolls are thicker on the right and thinner near the left wall. The above discussion explains the presence of DDLs having a somewhat zigzag pattern, as captured using all the three nonintrusive imaging techniques explored in the present work.

The whole field experimental data has been further made use of to illustrate the sense of fluid movement associated with DDLs (and interfaces) and the possible density profiles existing along the height of the observation area. While the PIV data has been made use of for understanding the fluid movement at any given vertical section of the observation area, the density profiles have been retrieved through the rainbow-schlieren images. Following this, Fig. 17(a) shows the  $x$  and  $y$  components of fluid velocities ( $V_x$  and  $V_y$ ) once the DDLs are developed in the liquid region and the schlieren-based density variation across the height of the fluid domain has been presented in Fig. 17(b). The alternating positive and negative tendency of velocity in Fig. 17(a) clearly establishes the circulation associated with DDLs, while a definite stepped structure with alternate high and low gradients, indicating the existence of a staircaselike structure, is evident from the density profile [Fig. 17(b)]. Low-density gradients correspond to the homogenization due to convective mixing inside DDLs, while high gradients correspond to the diffusive interfaces. A parallel shear flow

exists on the interfaces of DDLs and the fluid particles move towards the plume at the bottom of each diffusive interface and away from the plume at the top.

### B. Analytical scaling

Nondimensional Rayleigh numbers can be defined to characterize the fluid flow in buoyancy-driven flows. Two Rayleigh numbers  $Ra_S$  and  $Ra_T$  have been defined as solutal Rayleigh number and thermal Rayleigh number, respectively. The solutal Rayleigh number has been expressed as [26]

$$Ra_S = \frac{\beta_S g \left( \frac{\Delta C}{\Delta z} \right) l^4}{\alpha_S \nu}, \quad (1)$$

where  $\frac{\Delta C}{\Delta z}$  is the vertical compositional gradient,  $\beta_S$  is the solutal coefficient of expansion,  $\alpha_S$  is the solutal diffusivity, and  $\nu$  is the kinematic viscosity. As the lateral gradients occur due to the temperature difference between cooler plumes and the farther fluid near the wall, the appropriate length scale would be the distance between plume and wall. For the general analysis purpose, the length scale  $l$  has been taken as half of the breadth of the solidification chamber. Also, the thermal Rayleigh number has been defined as [26]

$$Ra_T = \frac{\beta_T g (\Delta T) l^3}{\alpha_T \nu}, \quad (2)$$

where  $\Delta T$  is the horizontal temperature difference,  $\beta_T$  is the thermal coefficient of expansion, and  $\alpha_T$  is the thermal diffusivity. The onset of DDLs has been estimated in the form of critical solutal and thermal Rayleigh numbers. Using the value of vertical compositional gradient ( $\frac{\Delta C}{\Delta z}$ ) at the onset of DDLs, as retrieved through interferometric analysis, the  $Ra_S$  value for water-28 wt.%  $\text{NH}_4\text{Cl}$  at the onset of DDLs has been determined to be as  $1.2 \times 10^7$  [using Eq. (1)]. The double-diffusive phenomenon is a bulk transport phenomenon, where  $Ra_S$  is expressed based on the compositional gradient exposed vertically and  $Ra_T$  is expressed on the basis of horizontal temperature difference. Young and Rosner [26] have established a relationship between the critical thermal Rayleigh number required for the onset of instability and different solutal Rayleigh number for a range of diffusivity ratios. The diffusivity ratio defined here is the ratio of solute Prandtl number and thermal Prandtl number or the ratio of thermal diffusivity to the solutal diffusivity:

$$\text{Diffusivity ratio, } H = \frac{Pr_S}{Pr_T} = \frac{\alpha_T}{\alpha_S}. \quad (3)$$

According to the relationship established by Young and Rosner [26], the critical thermal Rayleigh number ( $Ra_T$ ) at the onset of instability has been determined as  $2.6 \times 10^5$ . Using the relation of thermal Rayleigh number [Eq. (2)], the horizontal temperature difference at the corresponding time instant has been calculated as  $1.06^\circ\text{C}$ . The temperature difference between the fluid in the vicinity of the plume and near the sidewall was recorded experimentally using thermocouples and was found as  $1.5^\circ\text{C}$  on the top of the cell.

The strength of convection driven by the horizontal thermal transport is restricted by the vertical compositional gradient and hence both the mechanisms compete with each other. These competing mechanisms can be mathematically expressed as [11,27]

$$h_{\text{DDL}} \beta_S \left( \frac{\Delta C_V}{\Delta y} \right) = \beta_T \Delta T_H, \quad (4)$$

where  $h_{\text{DDL}}$  is the height of DDL,  $\left( \frac{\Delta C_V}{\Delta y} \right)$  is the vertical compositional gradient, and  $\Delta T_H$  is the horizontal temperature difference. With  $\Delta T_H$  calculated through Eq. (2), the height of DDLs has been determined to be 8.4 mm. The height of the DDLs by using the experimental observations made at the same time instant has been found as 6.3 mm, which gradually increases with time. These theoretically calculated scales and the experimental values, though not identical, show a reasonably good match with each other.

The overall vertical density variation (due to the coupled effects of thermal and composition gradients) at any given time instant can be calculated as

$$\Delta\rho_V = -\beta_T \Delta T_V + \beta_S \Delta C_V, \quad (5)$$

where  $\Delta T_V$  is the vertical thermal variation and  $\Delta C_V$  is the vertical solutal variation. Following Eq. (5), total density variation has been calculated as  $0.00494 \text{ g/cm}^3$ .

The downward velocity of DDLs can be validated by comparing the mass transfer by plumes from bottom to top with the bulk mass transfer in the form of DDLs that move from top to bottom. The formulation can be written as

$$A_{\text{DDL}} S_{\text{DDL}} = N a_{\text{plume}} V_{\text{plume}}, \quad (6)$$

where  $A_{\text{DDL}}$  is the cross-sectional area covered by DDLs and  $S_{\text{DDL}}$  is the analytical velocity calculated using the above relation. The scale of the downward velocity of DDL is calculated as  $0.008 \text{ mm/s}$  and the value determined through experiments is  $0.007 \text{ mm/s}$ .

During the salt finger convection, the scale of unstable perturbations can be characterized by a critical dimensional wave number, wherein the thermal and solutal gradients are the destabilizing and stabilizing components, respectively [15,31]. Using the same correlation, the scale of diameter of the solute driven plume has been determined, as shown in Eq. (7). The scale of solutal convection velocity of the plume has been formulated and shown in Eq. (8) [31,48]. Along with the scales of plume diameter and velocity, different relations were developed for the timescales of (i) mass transfer through the plume; (ii) downward motion of DDLs; (iii) heat transfer around the plume and are expressed through Eqs. (9)–(11), respectively. To obtain the scales of natural convection, buoyancy-driven convection relation for velocity scale has been expressed in Eq. (12), where  $h_l$  is the height of liquid above the mushy region:

$$d \sim 2\pi \left( \frac{\alpha_S v}{g\beta_S \left( \frac{\Delta C}{h_l} \right)} \right)^{1/4} = 0.35 \text{ mm}, \quad (7)$$

$$V_{\text{plume}} \sim \frac{Ra_S^{0.5} \alpha_S}{h_l} = 0.47 \text{ mm/s}, \quad (8)$$

$$t_{\text{plume}} \sim \frac{h_l}{V_{\text{plume}}} = 94.5 \text{ s}, \quad (9)$$

$$t_{\text{DDL}} \sim \frac{h_{\text{DDL}}}{S_{\text{DDL}}} = 750 \text{ s}, \quad (10)$$

$$t_{\text{heat\_diffusion\_plume}} \sim \frac{d^2}{\alpha_T} = 7.4 \text{ s}, \quad (11)$$

$$V_{\text{scale}} \sim \sqrt{\beta_S g \Delta C h_l} = 17 \text{ mm/s}. \quad (12)$$

The analytical values of plume diameter and plume velocity compare well with the experimentally determined values. Experimentally, the plume diameter has been obtained through schlieren observations (around  $1 \text{ mm}$ ) using an average pixel count. The velocity of plumes is determined by using both schlieren (around  $1.5 \text{ mm/s}$ ) and PIV (around  $0.6 \text{ mm/s}$ ) experiments. The velocity of the plume determined by PIV is relatively lesser ( $0.6 \text{ mm/s}$ ) in comparison. This mismatch may be attributed to the lesser number of tracer particles that get illuminated in the plume region. The presence of fewer particles in the plume region is expected to lead to errors in the PIV-based velocity measurements.



## V. CONCLUSION

Experiments to elucidate the plausible mechanisms responsible for the development of solute fingers, plumes, and double-diffusive layers (DDLs) during unidirectional solidification of  $\text{NH}_4\text{Cl}$  solution (water-28 wt.%  $\text{NH}_4\text{Cl}$ ) were reported. A one-on-one correspondence between the convective flow field and transported parameters was established through the application of a combination of nonintrusive measurement techniques. To the best of our knowledge, the work reported the very first attempt to simultaneously map the whole field distributions of temperature and compositional fields during the unidirectional solidification of such binary solutions using the concept of dual-wavelength interferometry. Various subprocesses involving a range of convective flow patterns that lead to the formation of the stepped structure of solutal and thermal gradients were visualized through rainbow-schlieren deflectometry. The associated flow velocities of solute fingers, plumes, and fluid inside DDLs were quantitatively mapped using PIV. The spatiotemporally resolved measurements made through gradients-based imaging techniques in conjunction with PIV successfully brought out some of the important mechanisms that characterize the unidirectional solidification of  $\text{NH}_4\text{Cl}$ -water binary mixtures. Plausible reason(s) explaining the formation and evolutionary stages of DDLs were discussed. Critical values of solutal and thermal Rayleigh numbers at the onset of DDLs were quantified as  $Ra_S = 1.2 \times 10^7$  and  $Ra_T = 2.6 \times 10^5$ , respectively. Experiments showed that DDLs originate in the form of convection rolls near sidewalls of the test chamber. These convection rolls near the opposite sidewalls, having an opposite sense of rotation, ultimately merge to form the DDLs that stretch throughout the breadth of the test chamber. The magnitude of fluid velocities inside the convective rolls was found to be in the range of  $10^{-4}$  (at the onset of convection rolls) to  $10^{-6}$  m/s (at the end of the experiment). DDLs were found to have a downward inclination towards the location of the plumes, thus exhibiting a slanted tilt. Adjacent layers of DDLs had an alternate sense of rotation, an aspect that was explained on the basis of observations made through the combination of imaging techniques employed. Several other characteristics like the downward movement of DDLs, origin of new DDLs from the top, size, shape, and orientation at different instants of time were investigated. A double flow structure of plumes and DDLs was established wherein each of these phenomena acts as a source to the other, as a consequence of which the DDLs were found to exist even after the completion of the solidification process. The analytical scales of various flow parameters such as the plume velocity and its diameter, the height of the double-diffusive layers, the downward velocity of DDLs, etc. were in close agreement with those determined through experiments. It is expected that the detailed understanding of the plausible mechanisms responsible for the formation of double-diffusively driven instability and the subsequent transient evolution of DDLs during unidirectional solidification of aqueous binary solutions, as developed through the present work, would be useful in a range of applications.

## ACKNOWLEDGMENT

The authors acknowledge the financial support from the Department of Science and Technology (DST), India (Grants No. EMR/2015/001140 and No. RD/0119-DST0000-007).

## APPENDIX: DATA REDUCTION METHODOLOGY FOR DUAL-WAVELENGTH INTERFEROMETRY

Simultaneous determination of whole field concentration and temperature fields has been carried out using the dual-wavelength interferometry technique. The density variation due to the coupled effect of compositional and thermal variations gets manifested in the form of a two-dimensional intensity field consisting of fringe patterns. Steps followed for the quantitative analysis of the

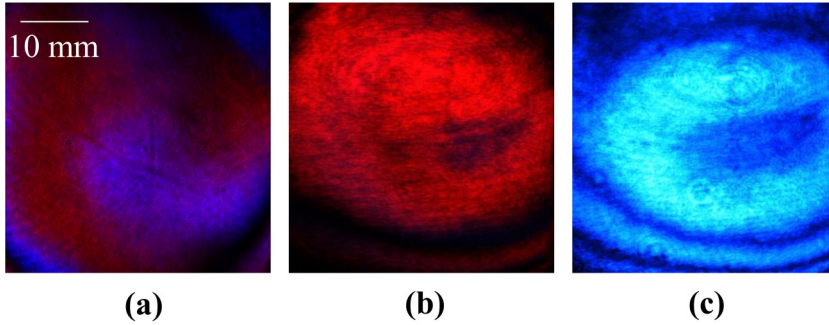


FIG. 18. Infinite fringe setting: (a) combined interferogram of red and blue, (b) corresponding red interferogram, and (c) corresponding blue interferogram.

dual-wavelength interferograms have been briefly presented below:<sup>1</sup> The combined interferograms of wavelengths  $\lambda_1 = 632.8 \text{ nm}$  and  $\lambda_2 = 457.9 \text{ nm}$  have been decomposed into two separate interferograms corresponding to each wavelength. As discussed in the experimental details of dual-wavelength interferometry, a Bayer mosaic color CCD camera has been used to record the interferograms. The CCD camera has a chip consisting of color-sensitive pixels arranged in the form mosaic pattern, which stores the information of the image digitally in the stacked color channels (red, green, and blue). Thus, the information regarding the two wavelengths can be obtained by separating the respective color channels of the recorded combined interferogram. Both separated interferograms represent the path-averaged density variation that occurred due to the combined effect of compositional and thermal gradients. The resultant intensity field consists of sinusoidal variations of bright and dark bands, known as fringes. The fringes in the interferograms constitute the locus of points with constant optical path length changes, which are averaged over the thickness of the chamber along the direction of the propagation of the light beam. A representative color interferogram recorded for the infinite fringe setting during the experiments has been shown in Fig. 18(a). Figure 18(b) shows the separated fringe pattern corresponding to red wavelength and Fig. 18(c) shows the separated fringe pattern corresponding to blue wavelength. The intensity of each color identified by the color sensor is stored in the form of a 2D matrix of integers containing grayscale resolution in the range of 0–255 in their corresponding color channels. The dark fringes represent the locus of identical optical path lengths, which are representatives of minimum intensity points (due to destructive interference). Once the two interferograms have been separated, the phase corresponding to each fringe pattern needs to be calculated. For calculating the phase information from the corresponding interferograms, a Matlab code has been developed. Using the dual-wavelength interferometer, the fringe orders corresponding to two distinct interferograms generated from two different wavelengths can be related to the temperature and concentration changes as per the following equations:

$$\left( \frac{\lambda\phi}{2\pi L} \right)_1 = \left( \frac{\partial n}{\partial C} \right)_1 \Delta C + \left( \frac{\partial n}{\partial T} \right)_1 \Delta T, \quad (\text{A1})$$

$$\left( \frac{\lambda\phi}{2\pi L} \right)_2 = \left( \frac{\partial n}{\partial C} \right)_2 \Delta C + \left( \frac{\partial n}{\partial T} \right)_2 \Delta T, \quad (\text{A2})$$

where  $\phi$ ,  $L$ ,  $\Delta C$ , and  $\Delta T$ , respectively, refer to the phase values, depth of test chamber (along the direction of propagation of beam), concentration change, and temperature change with respect to

<sup>1</sup>Authors' experience with the application of dual-wavelength interferometry technique and the details of associated data reduction methodology may be seen in [45].

the reference values. Here the superscripts 1 and 2 refer to the two different wavelengths, i.e.,  $\lambda_1$  and  $\lambda_2$ ;  $\frac{\partial n}{\partial C}$  and  $\frac{\partial n}{\partial T}$  represent the sensitivities of refractive index with respect to concentration and temperature, respectively. To solve the above set of equations, refractive index relations as a function of temperature and concentration are required. The refractive index gradients with concentration and temperature for different alloys at different wavelengths have been obtained using the Abbemat refractometer.

The top of the cell has been considered as the reference location, where the concentration and temperature values are known at different time instants. Temperature has been recorded on top using a thermocouple attached through the sidewalls, and the composition has been determined by extracting a small sample of solution from the top. The extracted fluid volume is used to determine the fluid refractive index on the top of the test cell using an Abbemat multiwavelength refractometer. Once the refractive index of any given sample is known at a particular temperature, the composition of that sample can be determined using the relation between variation of refractive index with composition at constant temperature. After obtaining the values of  $\Delta T$  and  $\Delta C$ , whole field temperature and concentration values at any given spatial location ( $i, j$ ) can be obtained by adding reference temperature and concentration values:

$$C(i, j) = C_{\text{ref}} + \Delta C(i, j), \quad (\text{A3})$$

$$T(i, j) = T_{\text{ref}} + \Delta T(i, j). \quad (\text{A4})$$

- 
- [1] S. M. Copley, A. F. Giamei, S. M. Johnson, and M. F. Hornbecker, The origin of freckles in unidirectionally solidified castings, *Metall. Trans.* **1**, 2193 (1970).
- [2] S. Tait and C. Jaupart, Compositional convection in a reactive crystalline mush, *J. Geophys. Res.* **97**, 6735 (1992).
- [3] D. Vikas, S. Basu, and P. Dutta, In-situ measurements of concentration and temperature during transient solidification of aqueous solution of ammonium chloride using laser interferometry, *Int. J. Heat Mass Transf.* **55**, 2022 (2012).
- [4] M. G. Worster, Convection in mushy layers, *Annu. Rev. Fluid Mech.* **29**, 91 (1997).
- [5] C. F. Chen and F. Chen, Experimental study of directional solidification of aqueous ammonium chloride solution, *J. Fluid Mech.* **227**, 567 (1991).
- [6] S. Tait, K. Jahrling, and C. Jaupart, The planform of compositional convection and chimney formation in a mushy layer, *Nature (London)*. **359**, 406 (1992).
- [7] H. E. Huppert, M. A. Hallworth, and S. G. Lipson, Solidification of  $\text{NH}_4\text{Cl}$  and  $\text{NH}_4\text{Br}$  from aqueous solutions contaminated by  $\text{CuSO}_4$ : The extinction of chimneys, *J. Cryst. Growth*. **130**, 495 (1993).
- [8] G. Amberg and G. M. Homsy, Nonlinear analysis of buoyant convection in binary solidification with application to channel formation, *J. Fluid Mech.* **252**, 79 (1993).
- [9] C. A. Middleton, C. Thomas, A. De Wit, and J.-L. Tison, Visualizing brine channel development and convective processes during artificial sea-ice growth using schlieren optical methods, *J. Glaciol.* **62**, 1 (2016).
- [10] J. S. Turner and H. Stommel, A new case of convection in the presence of combined vertical salinity and temperature gradients, *Proc. Natl. Acad. Sci. USA* **52**, 49 (1964).
- [11] S. A. Thorpe, P. K. Hutt, and R. Soulsby, The effect of horizontal gradients on thermohaline convection, *J. Fluid Mech.* **38**, 375, (1969).
- [12] C. F. Chen, D. G. Briggs, and R. A. Wirtz, Stability of thermal convection in a salinity gradient due to lateral heating, *Int. J. Heat Mass Transf.* **14**, 57 (1971).
- [13] T. Radko, A mechanism for layer formation in a double-diffusive fluid, *J. Fluid Mech.* **497**, 365 (2003).
- [14] Y. M. Chen and C. K. Liu, A holographic interferometry study of the double-diffusive layered system, *Exp. Heat Transf.* **10**, 67 (1997).

- [15] P. G. Baines and A. E. Gill, On thermohaline convection with linear gradients, *J. Fluid Mech.* **37**, 289 (1969).
- [16] J. S. Turner, The behaviour of a stable salinity gradient heated from below, *J. Fluid Mech.* **33**, 183 (1968).
- [17] J. S. Turner, Double-diffusive phenomena, *Annu. Rev. Fluid Mech.* **6**, 37 (1974).
- [18] M. E. Stern, Collective instability of salt fingers, *J. Fluid Mech.* **35**, 209 (1969).
- [19] M. E. Stern and J. S. Turner, Salt fingers and convecting layers, *Deep. Res. Oceanogr. Abstr.* **16**, 497 (1969).
- [20] R. W. Schmitt, Double diffusion in oceanography, *Annu. Rev. Fluid Mech.* **26**, 255 (1994).
- [21] W. J. Merryfield, Origin of thermohaline staircases, *J. Phys. Oceanogr.* **30**, 1046 (2000).
- [22] J. E. Hart, On sideways diffusive instability, *J. Fluid Mech.* **49**, 279 (1971).
- [23] J. E. Hart, Finite amplitude sideways diffusive convection, *J. Fluid Mech.* **59**, 47 (1973).
- [24] S. Thangam, A. Zebib, and C. F. Chenj, Transition from shear to sideways diffusive instability in a vertical slot, *J. Fluid Mech.* **112**, 151 (1981).
- [25] C. Beaume, Transition to doubly diffusive chaos, *Phys. Rev. Fluids* **5**, 103903 (2020).
- [26] Y. Young and R. Rosner, Linear stability analysis of doubly diffusive vertical slot convection, *Phys. Rev. E* **57**, 1183 (1998).
- [27] O. S. Kerr, Double-diffusive instabilities at a vertical sidewall after the sudden onset of heating, *J. Fluid Mech.* **909**, A11 (2020).
- [28] J. J. Feng and Y. N. Young, Boundary conditions at a gel-fluid interface, *Phys. Rev. Fluids* **5**, 124304 (2020).
- [29] C. S. Magirl and F. P. Incropera, Flow and morphological conditions associated with unidirectional solidification of aqueous ammonium chloride, *J. Heat Transfer* **115**, 1036 (1993).
- [30] C. Beckermann and R. Viskanta, Double-diffusive convection during dendritic solidification of a binary mixture, *Physicochem. Hydrodyn.* **10**, 195 (1988).
- [31] V. Kumar, A. Srivastava, and S. Karagadde, Compositional dependency of double-diffusive layers during binary alloy solidification: Full-field measurements and quantification, *Phys. Fluids* **30**, 113603 (2018).
- [32] S. N. Tewari and R. Tiwari, A mushy-zone Rayleigh number to describe interdendritic convection during directional solidification of hypoeutectic Pb-Sb and Pb-Sn alloys, *Metall. Mater. Trans. A* **34**, 2365 (2003).
- [33] J. C. Ramirez and C. Beckermann, Evaluation of a Rayleigh-number-based freckle criterion for Pb-Sn alloys and Ni-base superalloys, *Metall. Mater. Trans. A* **34**, 1525 (2003).
- [34] S. Karagadde, L. Yuan, N. Shevchenko, S. Eckert, and P. D. Lee, 3-D microstructural model of freckle formation validated using in situ experiments, *Acta Mater.* **79**, 168 (2014).
- [35] M. T. Rad, P. Kotas, and C. Beckermann, Rayleigh number criterion for formation of A-segregates in steel castings and ingots, *Metall. Mater. Trans. A* **44**, 4266 (2013).
- [36] V. Kumar, A. Srivastava, and S. Karagadde, Characteristics of solidification-driven double-diffusive layers in mixtures, *J. Flow Vis. Image Process.* **27**, 427 (2020).
- [37] V. Kumar, A. Srivastava, and S. Karagadde, Generalized regimes for the formation of stratified regions during freezing of multi-component mixtures, *Phys. Fluids* **31**, 123602 (2019).
- [38] F. Chen, Formation of double-diffusive layers in the directional solidification of binary solution, *J. Cryst. Growth* **179**, 277 (1997).
- [39] T. H. Solomon, Measurements of the temperature field of mushy and liquid regions during solidification of aqueous ammonium chloride, *J. Fluid Mech.* **358**, 87 (1998).
- [40] S. S. Varma, S. S. Rao, and A. Srivastava, Simultaneous measurement of thermal and solutal diffusivities of salt-water solutions from a single-shot dual wavelength interferometric image, *Exp. Therm. Fluid Sci.* **81**, 123 (2017).
- [41] P. Garaud, Double-diffusive convection at low Prandtl number, *Annu. Rev. Fluid Mech.* **50**, 275 (2018).
- [42] C. Ghenai, A. Mudunuri, C. X. Lin, and M. A. Ebadian, Double-diffusive convection during solidification of a metal analog system ( $\text{NH}_4\text{Cl-H}_2\text{O}$ ) in a differentially heated cavity, *Exp. Therm. Fluid Sci.* **28**, 23 (2003).

- [43] S. Narayan, A. Srivastava, and S. Singh, Rainbow schlieren-based investigation of heat transfer mechanisms during isolated nucleate pool boiling phenomenon: Effect of superheat levels, *Int. J. Heat Mass Transf.* **120**, 127 (2018).
- [44] A. Srivastava, Development and application of color schlieren technique for investigation of three-dimensional concentration field, *J. Cryst. Growth* **383**, 131 (2013).
- [45] S. S. Varma and A. Srivastava, Real-time two-color interferometric technique for simultaneous measurements of temperature and solutal fields, *Int. J. Heat Mass Transf.* **98**, 662 (2016).
- [46] F. Corvaro and M. Paroncini, Experimental analysis of natural convection in square cavities heated from below with 2D-PIV and holographic interferometry techniques, *Exp. Therm. Fluid Sci.* **31**, 721 (2007).
- [47] A. Srivastava, K. Murlidhar, and P. K. Panigrahi, Optical imaging and three dimensional reconstruction of the concentration field around a crystal growing from an aqueous solution: A review, *Prog. Cryst. Growth Charact. Mater.* **58**, 209 (2012).
- [48] E. M. Thompson and S. Julian, Mathematical and physical modelling of double- diffusive convection of aqueous solutions crystallizing at a vertical wall, *J. Fluid Mech.* **187**, 409 (1988).